JOURNAL OF GEOPHYSICAL RESEARCH: SOLID EARTH, VOL. 118, 1–13, doi:10.1002/jgrb.50286, 2013

Investigating the *P* wave velocity structure beneath Harrat Lunayyir, northwestern Saudi Arabia, using double-difference tomography and earthquakes from the 2009 seismic swarm

Samantha E. Hansen,[1] Heather R. DeShon,[2] Melissa M. Moore-Driskell,[3] and Abdullah M. S. Al-Amri[4]

Received 14 March 2013; revised 24 June 2013; accepted 9 July 2013.

[1] In 2009, a swarm of more than 30,000 earthquakes occurred beneath the Harrat Lunayyir lava field in northwest Saudi Arabia. This event was just one of several seismic swarms to occur in this region over the past decade. Surface deformation associated with the seismicity, modeled in previous studies using Interferometric Synthetic Aperture Radar (InSAR) data, is best attributed to the intrusion of a 10 km long dyke. However, little is known about the velocity structure beneath Harrat Lunayyir, making assessment of future seismic and volcanic hazards difficult. In this study, we use local double-difference tomography to generate a *P* wave velocity model beneath Harrat Lunayyir and to more precisely locate earthquakes from the 2009 seismic swarm. A pronounced fast velocity anomaly, centered at ~15 km depth with a shallower extension to the N-NW, is interpreted as an area of repeated magmatic intrusion. The crust surrounding the fast intrusion is slower than that suggested by broader-scale models for the Arabian Shield. The largest magnitude events occurred early in the swarm, concentrated at shallow depths (~2–8 km) beneath northern Harrat Lunayyir, and these events are associated with the dyke intrusion. Later, deep earthquakes (~15 km) beneath the southern end of the study region as well as a group of intermediate-depth events connecting the shallow and deep regions of seismicity occurred. These later events likely represent responses to the local stress conditions following the intrusion. Our results are unique since harrat magma systems are rarely imaged, and our observations, coupled with the seismic history in this region, suggest that future volcanic intrusions beneath Harrat Lunayyir are likely.

Citation: Hansen, S. E., H. R. DeShon, M. M. Moore-Driskell, and A. M. S. Al-Amri (2013), Investigating the *P* wave velocity structure beneath Harrat Lunayyir, northwestern Saudi Arabia, using double-difference tomography and earthquakes from the 2009 seismic swarm, *J. Geophys. Res. Solid Earth*, *118*, doi:10.1002/jgrb.50286.

1. Introduction

[2] Located in northwest Saudi Arabia, the Harrat Lunayyir volcanic field has experienced multiple seismic swarms over the past decade. Generally, the swarms are thought to reflect adjustments to tectonic stresses imparted on the region from rifting in the Red Sea and from strike-slip motion along the Gulf of Aqaba-Dead Sea transform fault (Figure 1). Asthenospheric flow beneath the Arabian Shield and crustal magmatic intrusions also contribute to the seismic activity [*El-Isa and Al-Shanti*, 1989; *Al-Amri*, 1995; *Pallister et al*., 2010; *Zobin et al*., 2011].

[3] In April–July 2009, a swarm of more than 30,000 earthquakes occurred beneath Harrat Lunayyir. Earthquake magnitudes (M) ranged from -0.7 to 5.4, and the total seismic moment release was ~5.3×10^{17} Nm [*Baer and Hamiel*, 2010]. Activity peaked on 19 May 2009, with a *M*5.4 event, and an 8 km long, NW trending surface rupture propagated across the northern section of the harrat (Figure 1). Minor structural damage was caused in the nearby town of Al Ays, and ~40,000 people were evacuated from the surrounding region. Analysis of Interferometric Synthetic Aperture Radar (InSAR) data has indicated that the associated surface deformation is best modeled by the intrusion of a 10 km long, vertical dyke with a ~340° strike and two NW-SE oriented normal faults which bound a 2–6 km thick, wedge-shaped graben that formed during the seismic swarm [*Baer and Hamiel*, 2010; *Pallister et al*., 2010]. A mixture of both high-frequency and very low-frequency earthquakes was observed during the swarm [*Pallister et al*., 2010], also consistent with volcanic intrusion [*Lahr et al*., 1994; *McNutt*, 1996].

[1]Geological Sciences Department, University of Alabama, Tuscaloosa, Alabama, USA.
[2]Huffington Department of Earth Sciences, Southern Methodist University, Dallas, Texas, USA.
[3]Department of Physics and Earth Science, University of North Alabama, Florence, Alabama, USA.
[4]Department of Geology and Saudi Society for Geosciences, King Saud University, Riyadh, Saudi Arabia.

Corresponding author: S. E. Hansen, Geological Sciences Department, University of Alabama, Box 870338, Tuscaloosa, AL 35487, USA. (shansen@geo.ua.edu)

2169-9313/13/10.1002/jgrb.50286

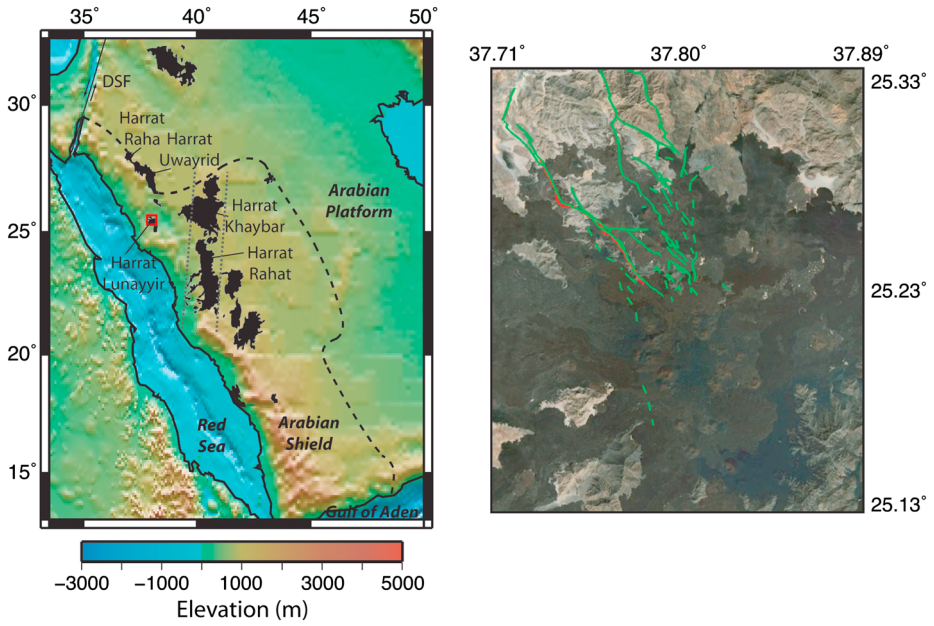

Figure 1. (left) Topography map of Saudi Arabia and surrounding regions. Harrat lava fields are labeled and highlighted in black. Gray dotted lines show the trend of the MMN volcanic line. Black dashed line marks the approximate boundary between the Arabian Shield and the Arabian Platform. DSF: Dead Sea Fault. Small red box marks the area shown in the map on the right. (right) Google Earth image of the Harrat Lunayyir region. Elevations across this area range from about -50 to 1700 m. Dark areas are basalt lavas and related pyroclastic deposits, and circular features are cinder cones. Red line marks the mapped surface rupture from *Pallister et al*. [2010]. Green lines mark faults and fractures mapped by *Jónsson* [2012]; dashed lines indicate fractures where displacement was less clear.

[4] Despite these observations, the seismic velocity structure beneath Harrat Lunayyir is largely unknown. While broader-scale velocity models of the Arabian Shield are available [e.g., *Mokhtar et al*., 1988; *Knox et al*., 1998; *Rodgers et al*., 1999; *Benoit et al*., 2003; *Julià et al*., 2003; *Park et al*., 2007], the local structure has important implications for the seismic and volcanic hazards in this region. Earthquake locations, the calculation of which is highly dependent on the velocity structure, often delineate important tectonic features of interest. In this study, we employ local double-difference (DD) tomography [*Zhang and Thurber*, 2003] to model the *P* wave velocity structure beneath Harrat Lunayyir and to refine earthquake locations associated with the 2009 seismic swarm. These constraints are not only important to understanding past periods of activity but also in accurately assessing future geologic hazards in this region.

2. Geologic Setting: Volcanic History, Seismicity, and Instrumentation

[5] The Arabian Peninsula consists of the western Arabian Shield and the eastern Arabian Platform (Figure 1). The Shield is composed of Proterozoic island arc terrains that were accreted together 600–900 Ma, and basement rocks in this region have little to no sediment cover. However, Proterozoic basement rocks in the Platform are covered by up to 10 km of Phanerozoic sediments [*Stoeser and Camp*, 1985]. At ~30 Ma, rifting processes started in Afar and propagated both eastward and northward to form the Gulf of Aden and the Red Sea, respectively [Figure 1; *Cochran and Martinez*, 1988; *Camp and Roobol*, 1992]. While seafloor spreading is occurring along the entire length of the Gulf of Aden [*Cochran*, 1981], the Red Sea displays a more complex pattern. Magnetic anomalies, GPS measurements, and normal fault earthquakes associated with rifting indicate that seafloor spreading is primarily occurring south of ~21°N at a rate of ~18 mm/yr. To the north, the Red Sea is underlain by stretched continental crust, and the rate of opening is only ~10 mm/yr [*Chu and Gordon*, 1998; *Cochran and Karner*, 2007; *ArRajehi et al*., 2010].

[6] Cenozoic tectonic activity associated with rifting in the Red Sea has led to uplift and volcanism throughout the Arabian Shield, resulting in extensive harrat lava fields that cover an area of ~180,000 km^2 [Figure 1; *Coleman et al*., 1983]. Two different phases of volcanism are recognized: 30–20 Ma tholeiitic eruptions that are associated with passive rifting of the Red Sea [*Almond*, 1986; *Coleman and McGuire*, 1988] and 14–12 Ma alkaline eruptions associated with the so-called West Arabian Swell, a N-S trending region of crustal uplift thought to be underlain by hot, upwelling mantle [*Camp and Roobol*, 1992; *Al-Saud*, 2008]. Most of the younger harrats lie along the Makkah-Medinah-Nafud (MMN; Figure 1) volcanic line, the central axis of the West Arabian Swell. However, NW oriented dykes [*Zahran et al*., 2002; *Johnson*, 2006] and NW-SE aligned vents in the volcanic fields [*Coleman et al*., 1983; *Camp and Roobol*, 1989, 1992; *Roobol*, 2009] are also common. No volcanic activity has occurred in the Arabian Platform. Two different sets of faults have also been recognized in northwestern Arabia, including a NE-SW trending system of Precambrian faults that

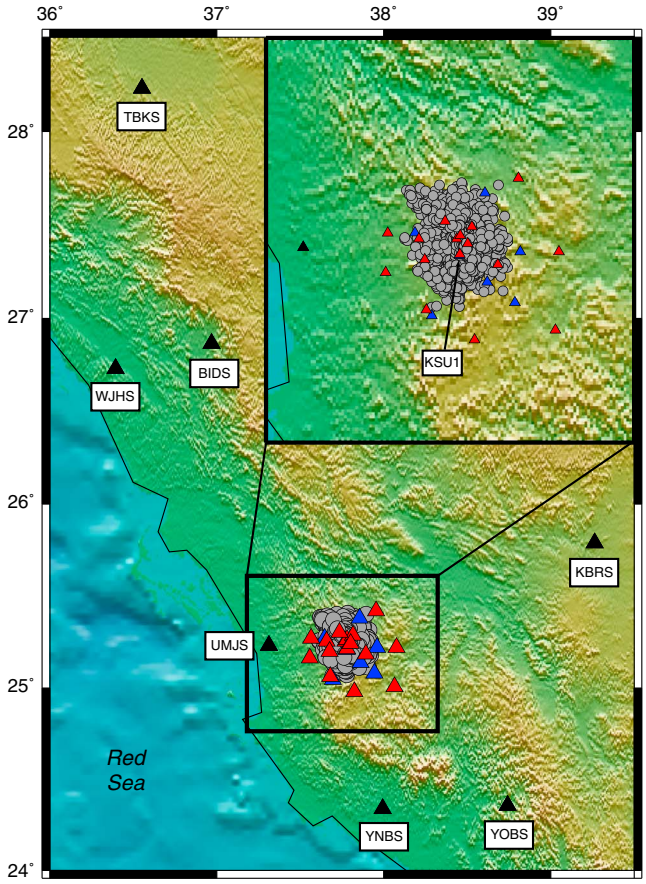

Figure 2. Station map with 30 s digital topography [*Wessel and Smith*, 1998]. Black, labeled triangles indicate broadband stations, which are part of the larger Saudi Arabian Seismic Network. Other triangles denote stations operated by the Saudi Geological Survey (blue) and stations operated by King Saud University and the King Abdulaziz City of Science and Technology (red). The inset on the upper right highlights the initial earthquake locations (gray circles), and data from these events were provided for analysis. The reference station (KSU1) for the minimum 1D VELEST modeling is also denoted in the inset.

were reactivated by rifting in the Red Sea and a NW-SE trending system subparallel to the rifting [*Mukhopadhyay et al*., 2012].

[7] Numerous studies have provided details on the broad-scale seismic structure of the Arabian Shield. Both *P* and *S* wave receiver functions [*Sandvol et al*., 1998; *Kumar et al*., 2002; *Al-Damegh et al*., 2005; *Tkalčić et al*., 2006; *Hansen et al*., 2007] as well as seismic refraction profiles [*Mooney et al*., 1985; *Prodehl*, 1985; *Gettings et al*., 1986] indicate an abrupt change in crustal thickness near the Red Sea, where the Moho depth changes from ~15 km near the coast to ~40 km further inland. This change occurs over a lateral distance of ~200 km [*Al-Damegh et al*., 2005]. However, the crustal thickness across the Arabian Shield then remains fairly constant, with the Moho at ~40–45 km. The lithospheric structure follows a somewhat similar trend, where the lithosphere-asthenosphere boundary deepens from ~40–50 km near the Red Sea to ~100–120 km beneath the Arabian Shield [*Camp and Roobol*, 1992; *Mooney et al*., 1985; *Altherr et al*., 1990; *Sandvol et al*., 1998; *Tkalčić et al*., 2006; *Hansen et al*., 2007]. Regional waveform modeling [*Rodgers et al*., 1999] has indicated that the average crustal *P* and S wave velocities (V_p and V_s) across the Arabian Shield are 6.42 and 3.70 km/s, respectively. This is consistent with receiver function analyses, which indicate the crustal V_p/V_s ratio beneath the Shield averages 1.76 [*Sandvol et al*., 1998; *Al-Damegh et al*., 2005]. Many seismic studies have shown that the upper mantle beneath the Arabian Shield and the Red Sea is anomalously slow, most likely associated with a broad thermal anomaly, with V_p and V_s of 7.90 and 4.30 km/s, respectively [*Knox et al*., 1998; *Rodgers et al*., 1999; *Debayle et al*., 2001; *Benoit et al*., 2003; *Julià et al*., 2003; *Nyblade et al*., 2006; *Tkalčić et al*., 2006; *Park et al*., 2007; *Hansen et al*., 2008; *Chang et al*., 2011].

[8] Harrat Lunayyir (Figure 1) is one of the smallest lava fields in the Arabian Shield, covering an area of ~3575 km^2, and it is situated on the passive margin adjacent to the northern Red Sea, where seafloor spreading is not developed. Previous studies have shown that during either early or long-term episodes of rifting, such margins often display magmatism and extension [*Pallister*, 1987; *Ebinger et al*., 2010; *LeTourneau and Olsen*, 2003]. Harrat Lunayyir contains more than 50 volcanic cones that follow a NW-SE trend [*Baer and Hamiel*, 2010; *Al-Amri et al*., 2012]. While the most recent volcanic eruption within the harrat was ~1000 years ago [*Camp et al*., 1987], the area displays geothermal features such as elevated groundwater temperatures and fumarole emissions [*Roobol et al*., 1994], and it has been suggested that this area is underlain by asthenospheric flow channelized northward from Afar [*Camp and Roobol*, 1992; *Hansen et al*., 2006; *Chang et al*., 2011]. Numerous NW-SE trending normal faults and tensional fractures have also been mapped across the Harrat Lunayyir region [Figure 1; *Jónsson*, 2012].

[9] In October 2007, a swarm of earthquakes occurred on the eastern edge of Harrat Lunayyir, but seismic instrumentation at the time was quite limited. When seismic activity resumed in April 2009, the regional network of broadband seismometers in Saudi Arabia was augmented with 29 local instruments operated by the Saudi Geological Survey (SGS), the King Abdulaziz City of Science and Technology (KACST), and King Saud University (KSU; Figure 2). Given the limited availability of broadband SGS data, most of our analysis is based on data from the 16 KACST and KSU stations, which were equipped with short-period, one-component (vertical) SS-1 Ranger seismometers with sampling rates of 100 samples per second (sps). Data for 5710 earthquakes, occurring between 30 April and 31 July 2009, were provided for analysis (Figure 2). It should be noted, however, that few events prior to the *M*5.4 main shock on 19 May 2009 are included because the full network of KACST and KSU stations was not completed until close to this date.

3. Methodology

3.1. Akaike Information Criteria (AIC) Picker

[10] Given the large quantity of data generated during the seismic swarm, it was not feasible to handpick all of the Harrat Lunayyir seismograms. Preliminary *P* wave picks were made using *taup_setsac* [*Crotwell and Owens*, 1998] and the ak135 Earth model [*Kennett et al*., 1995]. These

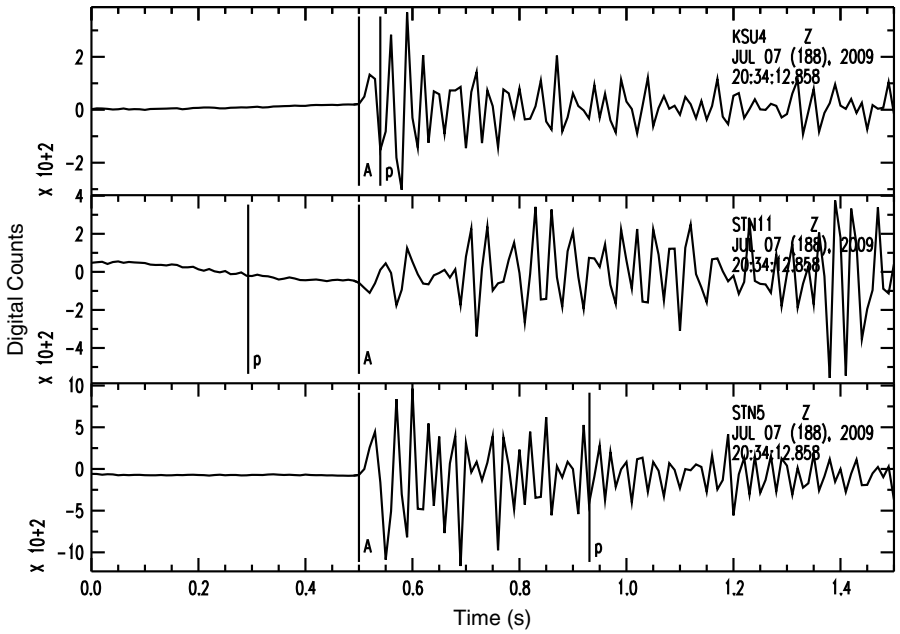

Figure 3. Examples of *P* wave picks made by the AIC phase picker [*Zhang et al*., 2003]. The three panels show the vertical component seismogram from three different Harrat Lunayyir stations (KSU4, STN11, and STN5) for a *M*0.1 event that occurred on 7 July 2009. Vertical lines denoted with "p" mark the predicted *P* wave arrival times determined by *taup_setsac* [*Crotwell and Owens*, 1998] using the ak135 reference model [*Kennett et al*., 1995]. Lines denoted with "A" are the *P* wave picks made by the AIC picker, and the waveforms have been aligned on this pick (with 0.5 s prior to and 1.0 s after the pick shown).

initial picks were then refined with the Akaike Information Criteria (AIC) phase picker developed by *Zhang et al*. (2003). Pronounced arrivals, such as the first arriving *P* wave, are detectable over a range of resolution scales while random noise decays and disappears. The AIC automatic picking algorithm applies a wavelet transformation to each seismogram through a series of sliding time windows. In each window, the autopicker is applied to the absolute wavelet coefficient. If the picks are consistent at three different scales, the phase arrival is marked within that time window (*Zhang et al*., 2003). The close station-event proximity and high signal-to-noise ratio of our data made it possible to acquire AIC picks for even small earthquakes. Figure 3 shows an example of the refined picks made using the AIC approach for a magnitude 0.1 event, which was later relocated with the joint inversion.

3.2. Waveform Cross-Correlation

[11] When two earthquakes are closely spaced and have similar source mechanisms, the ground motions generated by those two events should be very similar. This similarity can be exploited to obtain accurate differential times from the waveform data, which can be used to improve location results [*Got et al*., 1994; *Shearer*, 1997; *Rubin et al*., 1999; *Waldhauser et al*., 1999; *Waldhauser and Ellsworth*, 2002; *Schaff et al*., 2002]. The differential times can also be combined with absolute arrival times to model 3D velocity structure [*Zhang and Thurber*, 2003]. The relative time delay determined by cross-correlation (CC) techniques has an associated coefficient value, which varies between 0 and 1, where 1 indicates perfect waveform similarity. The CC coefficient will be reduced if the waveforms are less similar or if the signals are contaminated by noise. Often, only time delays with coefficients above a specific threshold are used for analysis to minimize the number of false-positive correlations [e.g., *Schaff et al*., 2002].

[12] Even for similar events, low CC coefficients can result from correlated or partially correlated noise originating from site effects and other constant noise sources (e.g., wind, cultural noise). On the other hand, such Gaussian noise may dominate the correlation estimate instead of the signal of interest, leading to high coefficients for dissimilar events [*Du et al*., 2004]. To avoid such potential issues, we have employed the bispectrum cross-correlation (BCC) approach, which suppresses Gaussian noise and accurately determines CC time delays. In the absence of correlated noise, the BCC technique generates time delay estimates comparable to other CC approaches [*Du et al*., 2004].

[13] Using the Bispectrum Cross-correlation package for SEISmology (BCSEIS), the time delays determined by traditional, first-order frequency domain CC are verified by computing a BCC-predicted lag adjustment for both filtered and unfiltered waveforms [*Du et al*., 2004]. Noise characteristics may vary between raw and filtered data, so this approach provides additional quality control. For a given event pair, if all three lags (i.e., traditional CC, unfiltered BCC, and filtered BCC) agree within some user-specified threshold, the traditional lag is considered verified and a differential time is computed. The CC coefficients for a specific event pair are also compared to those at all other recording stations. This can help identify cases where a low CC coefficient may result from site effects or a low signal-to-noise ratio [*Du et al*., 2004]. Three coefficient thresholds are set by the user: $CC^{lim(l)}$, CC^{lim}, and $CC^{lim(u)}$. All verified lags with

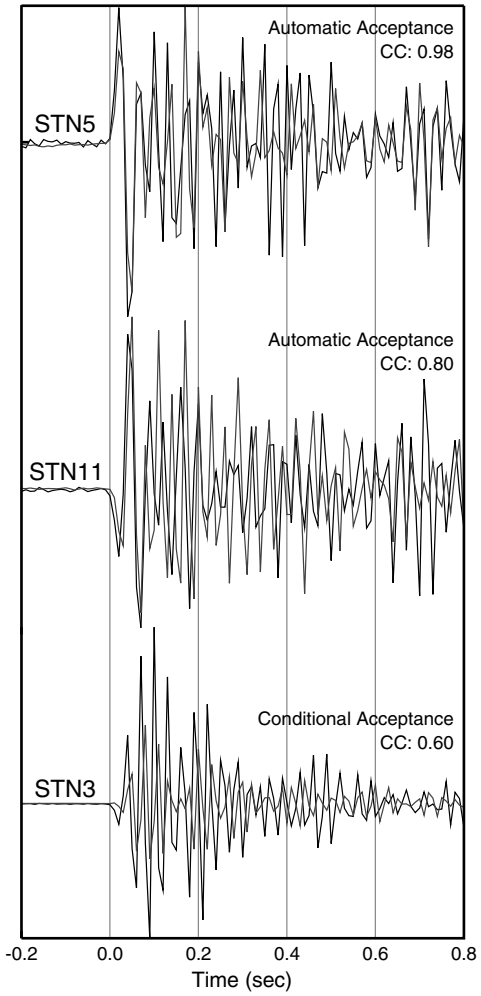

Figure 4. Examples of cross-correlated waveforms identified by BCSEIS [*Du et al*., 2004]. Event 1 (black waveforms) occurred on 23 May 2009, and event 2 (gray waveforms) occurred on 30 May 2009. Stations STN5 and STN11 both have CC coefficients ≥ 0.75, so the corresponding differential travel times are automatically accepted. Station STN3 has a lower CC coefficient, but because of the chosen values of $CC^{lim(u)} = 0.90$ and $CC^{lim(l)} = 0.50$, the differential travel time at this station is also accepted and is used for tomography.

CC coefficients ≥ CC^{lim} are used, similar to a traditional threshold approach. Additionally, if the CC coefficient ≥ $CC^{lim(u)}$ for at least one event pair at a recording station, then the CC coefficient only needs to be ≥ $CC^{lim(l)}$ for event-pair differential times at other stations to be accepted [*Du et al*., 2004].

[14] For the Harrat Lunayyir data set, the raw waveforms were filtered using a three-pole, two-pass, Hanning bandpass filter with corner frequencies at 0.25 and 20 Hz. CC was performed using a window that extended from 0.2 s before to 0.5 s after the P wave arrival determined by the AIC picker. This window size was large enough to CC the P wave coda to identify similar earthquakes but generally small enough to avoid CC of large amplitude, later arrivals. The BCSEIS verification threshold was set to two times the sampling interval, and the coefficient thresholds were set to 0.50, 0.75, and 0.90 for $CC^{lim(l)}$, CC^{lim}, and $CC^{lim(u)}$, respectively. These thresholds were chosen based on trial and error to maximize the number of differential times and to minimize the inclusion of poor quality data. Examples of CC event pairs identified by BCSEIS are shown in Figure 4.

3.3. Minimum 1D Starting Velocity Model

[15] Solutions to 3D local earthquake tomography result from linear approximations to nonlinear functions, usually solved by a linearized inversion. Due to this, the resulting tomographic images are dependent on the starting reference model and the quality of the initial hypocenter locations [*Michael*, 1988; *van der Hilst and Spakman*, 1989; *van der Hilst et al*., 1991]. If the initial model is too inaccurate, the output model may have artifacts that are difficult to identify and quantify. The best results are obtained using a starting model that is close to the true model, but this is often difficult to estimate.

[16] Previous studies [*Kissling et al*., 1984; *Kissling*, 1988] suggest jointly inverting travel time data to solve for a "minimum 1D model" [*Kissling*, 1988], which can then be used as the starting, reference model for 3D tomography. We have employed the method outlined by *Kissling et al*. [1994] to develop such a 1D model for Harrat Lunayyir using the VELEST program. To begin, an a priori 1D model was developed based on previous studies of the Arabian Shield including receiver function estimates, group velocities, and seismic refraction [*Mooney et al*., 1985; *Sandvol et al*., 1998; *Rodgers et al*., 1999; *Julià et al*., 2003; *Al-Damegh et al*., 2005]. Given its central location, station KSU1 (Figure 2) was chosen as the reference station. Upper crustal layers in the initial model are 2 km thick while lower crustal layers are 5 km thick. In developing the minimum 1D model, we used the highest quality events in the data set, which were those that had more than eight recorded arrivals and a maximum azimuthal separation (GAP) of less than 180°. Of the original data set, ~2000 earthquakes met this criterion. To ensure that the final 1D minimum model was not dependent on a particular subset of data, several different 500-event subsets were tested. Each subset was iteratively inverted for hypocenter locations and 1D velocity structure. Once no dependence was confirmed, one subset was used to refine the model using the trial-and-error process of *Kissling et al*. [1994]. Convergence occurred after about six iterations.

[17] Models that were slightly faster and slower than the a priori model were also examined to determine the dependence of the final minimum 1D model on the initial model choice. The general crustal velocities and thicknesses in the study region are relatively well known on a broad scale, so the fast and slow versions of the a priori model are not extreme in terms of expected petrological values. Rather, they serve as a range of possible values to test if convergence between the three starting models is obtained with the inversion scheme. Initial inversions with the a priori, fast, and slow starting models did not converge at depths below ~16 km. This is a result of the limited hypocenter depth distribution and station geometry. Almost all the recorded events had hypocenters at depths less than 16 km, and we are unable to resolve the velocity structure at depths where there are no crossing raypaths. Therefore, velocities below 16 km depth were damped to remain fixed, and with this constraint, all three starting models converged.

Table 1. Final Minimum 1D Velocity Model From VELEST

Vp (km/s)	Depth (km)
4.18	0.00
5.43	2.00
5.43	4.00
5.68	6.00
6.33	8.00
6.72	10.00
6.72	15.00
6.72	20.00
6.90	25.00
7.78	35.00
8.30	100.00
8.60	400.00

[18] The same VELEST inversion was performed with different 500-event subsets of the best-constrained data, and each produced similar results. No dependence on the starting 1D model was observed, and the final 1D minimum model is provided in Table 1. The 1D minimum model was also used to relocate all the events in the original data set (i.e., not just the best-constrained earthquakes). Of the original 5710 earthquakes, 732 events were lacking event or phase arrival information needed to be relocated, leaving 4978 events in the complete data set. The VELEST relocations for the best-constrained events (Figure 5) and the minimum 1D velocity model (Table 1) serve as the starting locations and reference model for the three-dimensional DD tomography.

3.4. Double-Difference Tomography

[19] In earthquake location methods, there is a strong coupling between event hypocenters and velocity structure [e.g., *Crosson*, 1976; *Aki and Lee*, 1976; *Ellsworth*, 1977; *Kissling et al*., 1984; *Thurber*, 1981; 1992]. Standard local earthquake tomography (LET) approaches use arrival time residuals to improve both event locations and velocity structure, but these techniques can be biased by pick time errors, leading to decreased resolution in the velocity model. Alternatively, the DD location approach uses differential times to determine relative earthquake locations. However, this technique only works well if the separation between earthquake pairs is small compared to the event-station distance and to the velocity heterogeneity scale length [*Waldhauser and Ellsworth*, 2000]. By neglecting 3D structure, the event locations can also be biased. The *tomoDD* method developed by *Zhang and Thurber* [2003] combines both the LET and DD approaches to minimize problems associated with both techniques. The simultaneous inversion of both absolute and differential travel times improves the accuracy of earthquake locations as well as the 3D velocity heterogeneity. Differential times, particularly when calculated with CC approaches like BCSEIS, minimize variations in the velocity model resulting from picking errors. To control the relative weighting of absolute and differential time data, a hierarchical weighting scheme is employed such that broader-scale velocity variations are first resolved with the absolute times and then the resolution is refined with the differential data

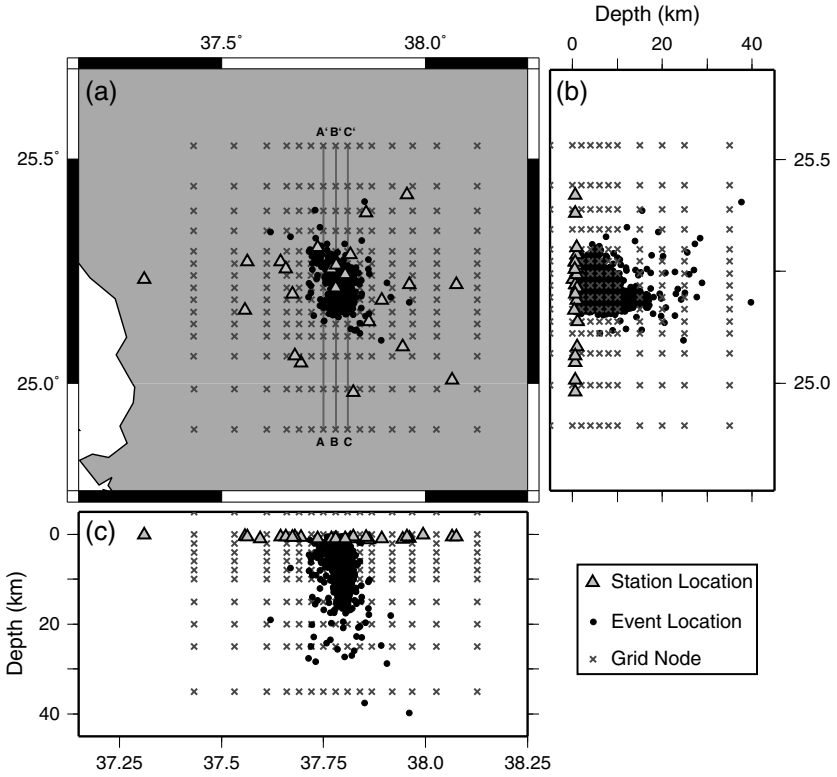

Figure 5. Input parameters for *tomoDD*. (a) Station and event locations are denoted by triangles and dots, respectively. Event locations are those obtained with VELEST and the minimum 1D velocity model. Grid nodes are denoted by gray crosses. Vertical gray lines labeled A-A', B-B', and C-C' denote profile locations shown in Figures 6 and 7. (b and c) Same data shown in cross section.

Table 2. Hierarchical Weighting Scheme Used With *tomoDD*

NITER[a]	WTCCP[b]	WRCC[c]	WDCC[d]	WTCTDTP[e]	WRCT[f]	WDCT[g]	WTCD[h]	DAMP[i]	JOINT[j]	THRES[k]
1	0.01	-9	-9	0.1	-9	-9	10	190	1	2
1	0.01	-9	-9	0.1	-9	-9	10	170	0	2
2	0.01	-9	-9	0.1	10	-9	10	170	1	2
2	0.01	-9	-9	0.1	10	-9	10	180	0	2
2	0.01	-9	-9	0.1	10	10	10	170	1	2
2	0.01	-9	-9	0.1	10	10	10	190	0	2
2	0.01	-9	-9	1	10	10	0.1	170	1	2
2	0.01	-9	-9	1	10	10	0.1	230	0	2
2	0.50	10	-9	1	8	8	0.1	170	1	3
2	0.50	10	-9	1	8	8	0.1	230	0	3
2	1.00	8	8	0.5	6	8	0.05	170	1	3
2	1.00	8	8	0.5	6	8	0.05	280	0	3
2	1.00	6	6	0.5	6	8	0.05	170	1	3
2	1.00	6	6	0.5	6	8	0.05	280	0	3

[a]NITER: Number of iterations for each weighting and inversion parameterization.
[b]WTCCP: Weight of CC-derived *P* wave differential times.
[c]WRCC: Factor multiplied by the standard deviation of all CC-derived differential times to identify outliers.
[d]WDCC: Maximum distance (km) between CC linked pairs.
[e]WTCTDTP: Weight of catalog *P* wave differential times.
[f]WRCT: Factor multiplied by the standard deviation of all catalog times to identify outliers.
[g]WDCT: Maximum distance (km) between catalog linked pairs.
[h]WTCD: Weight of catalog absolute travel times, multiplied by WTCTDTP.
[i]DAMP: Damping applied during nonlinear inversion.
[j]JOINT: 0, location calculation only. 1, joint inversion for velocity and location.
[k]THRES: Velocity at nodes with DWS values below this number is held fixed during the joint inversion.

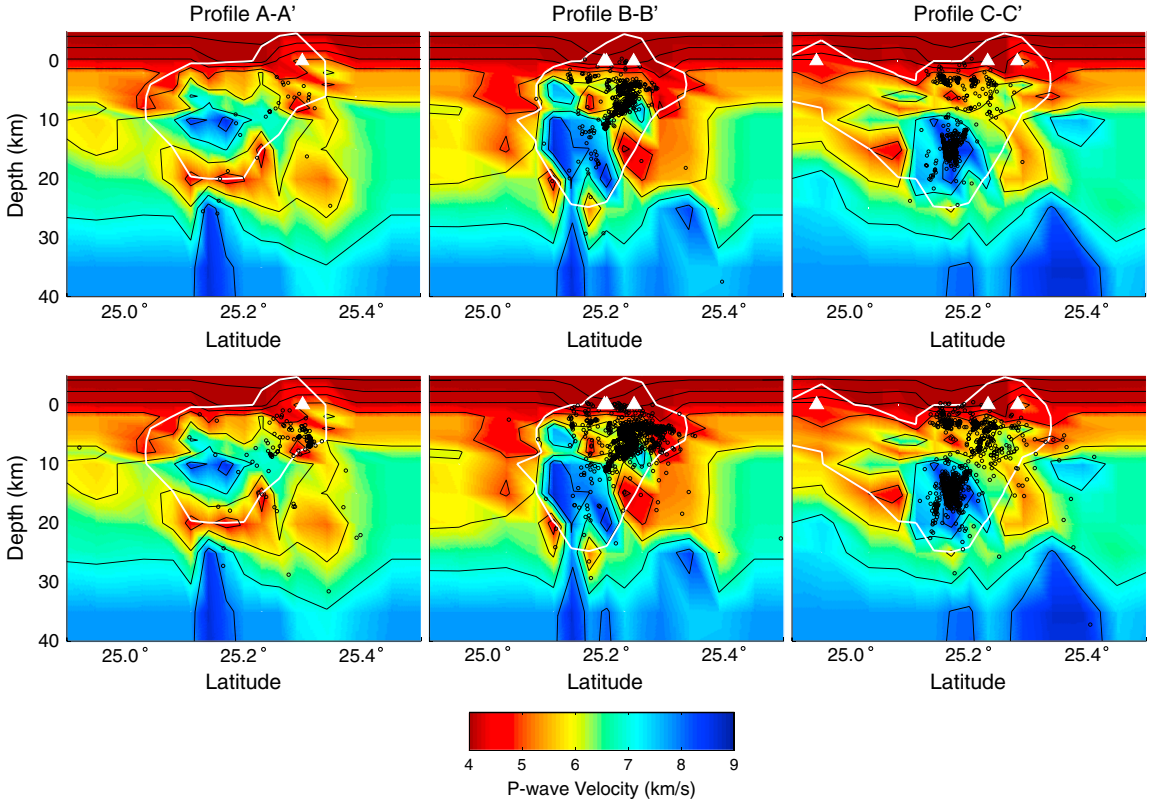

Figure 6. South-to-north cross sections through the 3D *P* wave velocity model. Profile locations are shown in Figure 5. Black lines are velocity contours with 1 km/s intervals. Thick white lines encompass nodes with DWS greater than 100; areas outside this line are expected to have reduced or no resolution. White triangles mark station locations and black circles mark event relocations. All depths are referenced to sea level. The top row shows the profiles with the best-constrained event relocations (that is, the events that were actually used in the *tomoDD* joint inversion). The bottom row shows the profiles with all event relocations, including events that were less well constrained. See text for additional details.

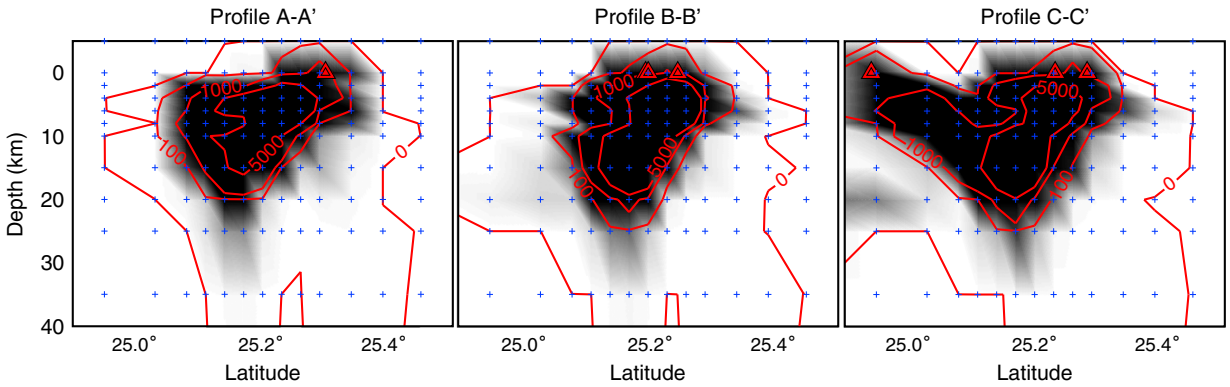

Figure 7. DWS contours along cross-sectional profiles. DWS is a weighted measure of the number of data sampling each volume represented by a grid node. Darker shading indicates higher DWS values, and red lines contour values of 0, 100, 1000, and 5000. Blue crosses mark grid nodes and red triangles denote stations along each profile. Given the rapid DWS increase inside the 100 contour, nodes with DWS greater than 100 were considered sufficiently resolved for interpretation.

(Table 2). We implement DD tomography using the publically available *tomoDD* (version 2.1) algorithm described by *Zhang and Thurber* [2003].

[20] Both velocity and station parameter damping affect the resulting velocity model and corresponding resolution estimates [*Kissling et al*., 2001], and appropriate damping parameters result in a smoothly varying model with minimum data variance [*Eberhart-Phillips*, 1986]. Trade-off curves corresponding to a range of damping (1–500) and smoothing (0.5–5.0) parameters were examined to determine which values minimized the data variance while maintaining low model variance. For *P* wave velocity, we selected an initial damping of 190 and smoothing in the x, y, and z directions of 2 for all inversion steps. Slightly reduced damping (170) in later iterations led to reduced RMS misfit. For location-only steps, damping values were chosen such that the condition number (CND), which is defined as the ratio of the largest to smallest eigenvalues, was between 40 and 80, following the work of *Waldhauser and Ellsworth* [2000]. CND has no meaning during the joint inversion steps [*Zhang and Thurber*, 2003].

[21] Grid spacing was chosen to minimize the variability in the number of raypaths that sample each node in the model (Figure 5). The catalog data (both absolute and differential times) used in the joint *tomoDD* inversion are optimized by the number of station recordings as well as the connectivity between events, which is established using a nearest-neighbor approach [*Waldhauser and Ellsworth*, 2000]. For the Harrat Lunayyir data set, we required each event to have at least eight neighboring events within a 20 km radius, and each event-pair had to have at least eight station recordings, similar to the constraints used in VELEST (see section 3.3). All of the best-constrained events from VELEST met these criteria, and these earthquake hypocenters, along with the associated 1D minimum velocity model, served as the starting point for our 3D inversion. Associated CC differential times were taken from our BCSEIS results. In total, 14,728 absolute catalog times, 202,243 differential catalog times, and 233,720 CC

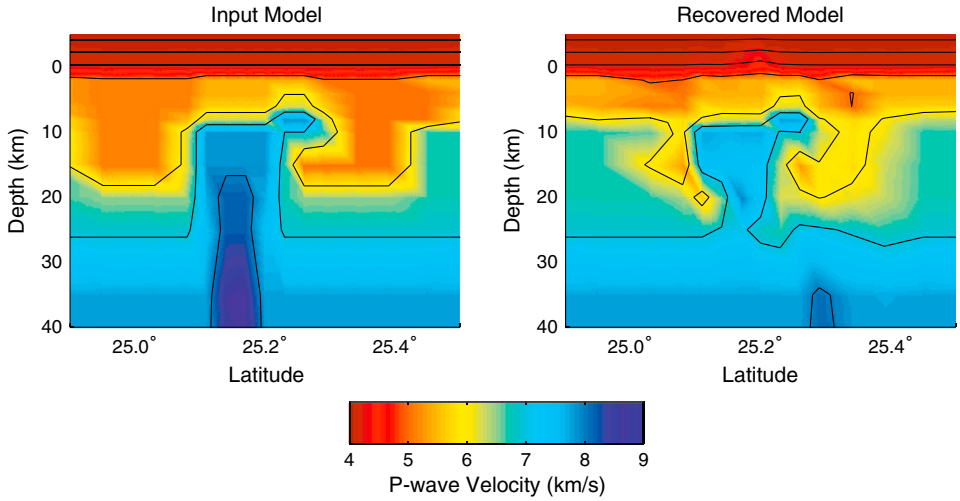

Figure 8. Synthetic velocity models. (left) The input model includes a fast anomaly centered at ~15 km depth, with a shallower extension (~9 km) to the N-NW and additional fast velocities extending to depth. Slow velocity anomalies surround the fast region. (right) The recovered model provides a good match to the major features observed in our tomographic results (Figure 6).

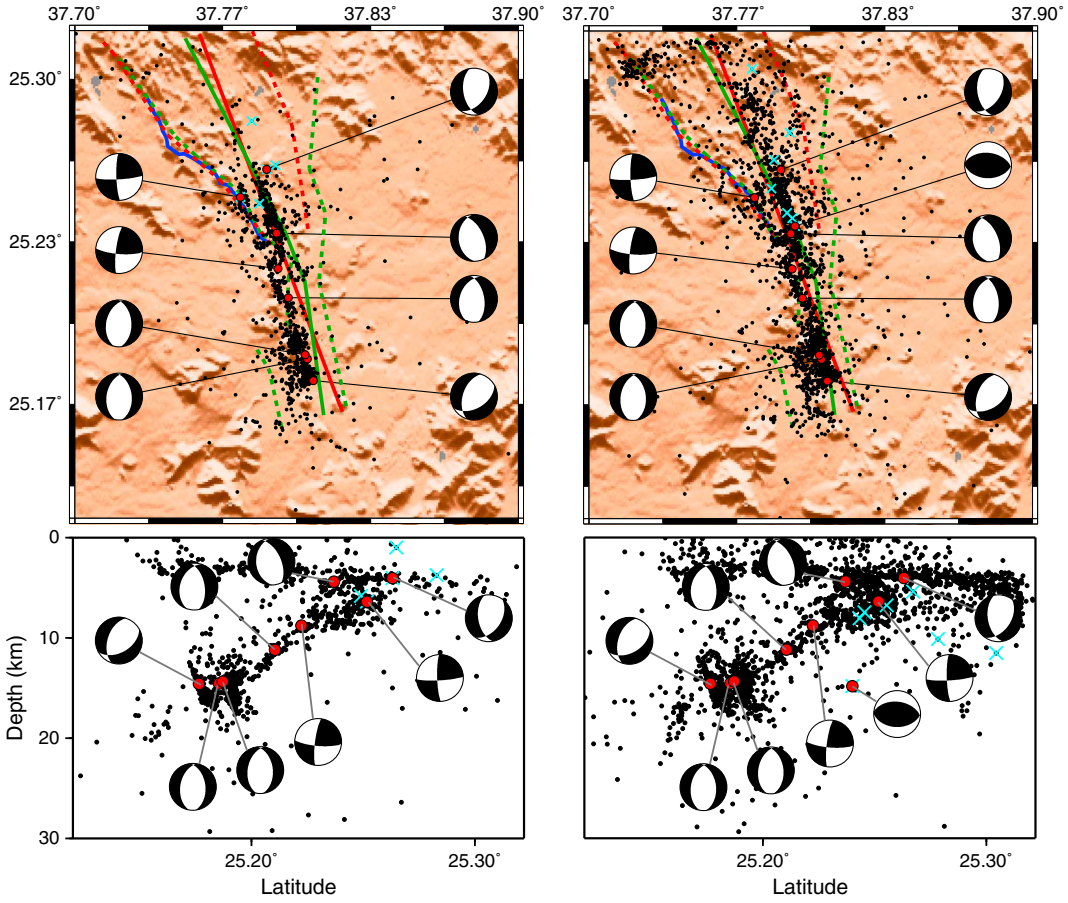

Figure 9. Event relocations from *tomoDD* (black dots) in both (top) map view and (bottom) cross section. Images on the left show the best-constrained events that were used in the *tomoDD* joint inversion. Images on the right show all relocated events, including those that were less well constrained. Cyan crosses mark events with magnitudes > 3.5. Red dots mark events (or event clusters) for which focal mechanisms were computed, and these mechanisms are shown along the sides of the plots. On the map view images, red and green lines denote the dyke (solid) and graben-bounding normal faults (dashed) inferred from InSAR modeling from the *Pallister et al.* [2010] and the *Baer and Hamiel* [2010] studies, respectively. Blue lines denote surface rupture mapped by *Pallister et al.* [2010]. The background of each image is a 3 s digital topography map [*Farr et al.*, 2007].

differential times were used in our joint inversion to solve for the *P* wave velocity structure.

[22] Also similar to VELEST, the final 3D velocity model generated with *tomoDD* was used to relocate the other, less-constrained earthquakes in our data set. Of the 4978 events relocated by VELEST, 2724 earthquakes met the *tomoDD* event criteria outlined above. While these events were not used to constrain the velocity structure beneath Harrat Lunayyir, their corresponding locations in relation to local tectonic features are of interest.

4. Results

4.1. Velocity Modeling Results

[23] Our *P* wave velocity model beneath Harrat Lunayyir is shown in Figure 6. These profiles highlight the majority of the event relocations and the best-resolved velocity features. Weighted RMS decreased from 0.624 to 0.024 s for the absolute and differential catalog data and from 0.324 to 0.008 s for the CC data following the joint inversion. A small number of events (30) were removed during the inversion either because they relocated as air quakes or because all associated arrivals failed residual weighting thresholds.

[24] A pronounced fast velocity anomaly is observed beneath Harrat Lunayyir, centered at ~15 km depth. From the different cross sections, it can be seen that this feature is ~6 km wide at its thickest point. The fast velocities also extend to somewhat shallower depths (~9 km) to the N-NW, and both of these fast regions coincide with a majority of the local seismicity. These regions of fast velocity are generally surrounded by slower velocities. The best-resolved nodes have derivative weighted sum (DWS) values ≥ 100 and are located between ~25.05°N and 25.35°N latitude and above ~20 km depth (Figures 6 and 7).

[25] A variety of conditional synthetic tests were examined to assess model resolution, evaluate smearing, and determine expected velocity recovery. Synthetic arrival times were calculated using the same hypocenters, weighting scheme, and ray coverage as the data used in our 3D inversion. Noise was randomly generated between ±0.05 s and was added to

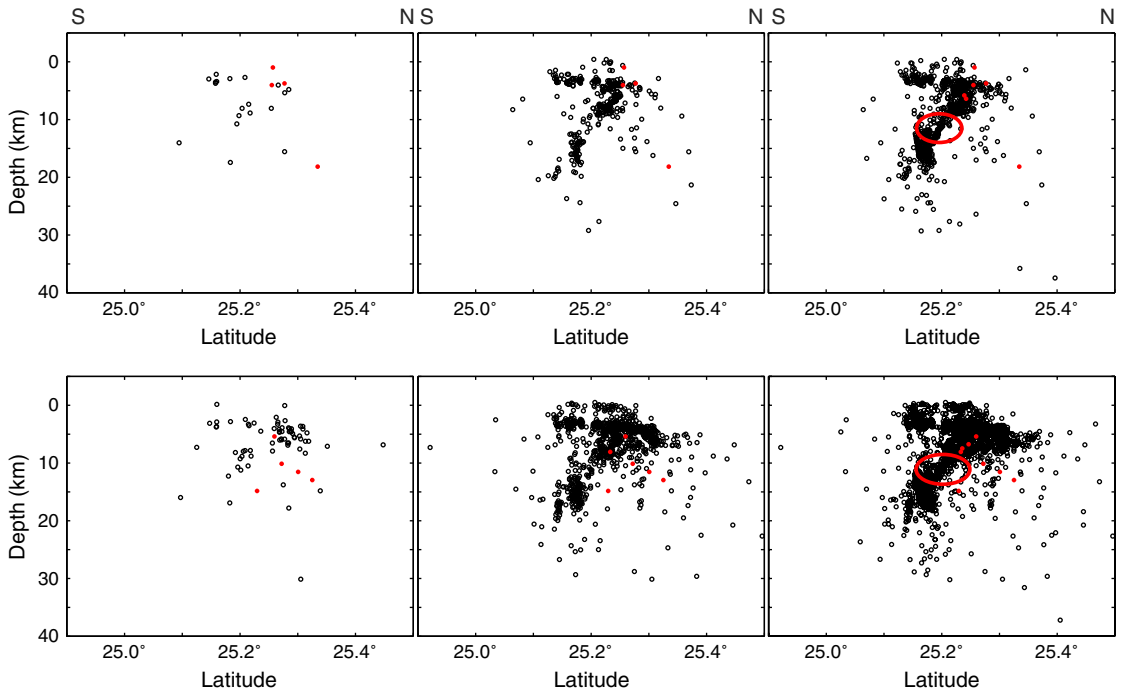

Figure 10. South-to-north cross sections showing earthquake relocations (black circles) as a function of time. Larger-magnitude (>3.5) events are highlighted by red dots. The top row shows the best-constrained event relocations (that is, the events that were actually used in the *tomoDD* joint inversion). The bottom row shows all event relocations, including events that were less well constrained. (left) Events through 27 May 2009; (center) events through 28 June 2009, (right) events through 31 July 2009. Red ellipses denote intermediate-depth earthquakes.

the synthetic travel times to conservatively estimate uncertainty. The synthetic data was then inverted using the same parameterization as that used for the real data. Figure 8 shows the synthetic velocity model that best mimics the major features observed in our tomographic results. The center of the fast anomaly, as well as the shallower N-NW extension, is well matched by our model. A conduit-like, fast extension at depth (~20–30 km) may also be present beneath Harrat Lunayyir (Figures 6 and 8), but since the model has lower DWS values at these depths, this feature is not well resolved.

4.2. Relocation Results

[26] Final event locations for the best-constrained events are shown in Figures 6, 9, and 10. In map view, the earthquakes define a NW-SE trend, extending from ~25.27°N to 25.23°N. The seismicity then appears to be slightly offset to the SW, where the linear trend continues to ~25.20°N. The southernmost events form a somewhat broader cluster (Figure 9). In cross section, shallow seismicity is concentrated between ~2 and 8 km depth. However, a distinct dipping trend of seismicity is observed, deepening to the S-SE, and the deepest earthquakes are concentrated at ~15 km depth. As mentioned previously, the earthquakes generally coincide with regions of fast velocity. The same seismicity trends and observations can be seen when all earthquake relocations are plotted, including those for the less-constrained events (Figures 6, 9, and 10).

[27] *TomoDD* does not formally calculate location uncertainties; therefore, we employ a bootstrap approach to estimate the associated error. *Baer and Hamiel* [2010] indicate that the original event locations have uncertainties of 0.5–1.0 km laterally and 0.8–1.5 km in depth. To be conservative, these uncertainty estimates were doubled. Each original earthquake location was randomly perturbed up to ±2 km laterally and ±3 km vertically, and these adjusted event locations were then relocated with our final 3D *P* wave velocity model using the same approach outlined previously. This was repeated 100 times for all earthquakes in our data set, and the average change in location and depth was computed. Based on this bootstrap approximation, our event locations are constrained to within 0.36 km laterally and 0.63 km in depth.

5. Discussion

[28] Modeling of InSAR data following the 2009 seismic swarm at Harrat Lunayyir has indicated that the local deformation is best attributed to the intrusion of a ~10 km long, NW trending dyke, extending from ~2 km below the surface down to ~8–10 km depth. The associated maximum opening is roughly 2–4 m at ~5 km depth, giving the dyke a volume of ~0.1 km^3 [*Baer and Hamiel*, 2010; *Pallister et al.*, 2010]. One might expect to see a low velocity anomaly associated with the intrusion, but our velocity model cannot laterally resolve such a narrow (2–4 m) feature. Therefore, the dyke has no velocity signature in our model. Additionally, no significant low velocity anomaly associated with a magma chamber beneath Harrat Lunayyir is observed. It has been suggested that volcanism beneath Harrat Lunayyir is fed by a deep magma source [*Camp et al.*, 1992; *Baer and*

Hamiel, 2010; *Zobin et al*., 2011]. Geochemical analysis has indicated that the majority of volcanic rocks in nearby harrat lava fields were not derived from primary magmas but rather from fractionated liquids that may have resided at moderate crustal depths [<28 km; *Camp et al*., 1992]. In other words, if a magma body is present, it is likely ponding at depths deeper than those resolved by our model (i.e., > 20 km).

[29] The region surrounding the InSAR-modeled dyke is instead marked by anomalously fast velocities at depth (Figure 6). It is not uncommon for dykes to repeatedly intrude a given area in the crust [e.g., *Dieterich*, 1988; *Payne et al*., 2009; *Ebinger et al*., 2010; *Chadwick et al*., 2011], and once solidified at depth, harrat magmas should have significantly higher velocities than the surrounding Precambrian rocks. High-velocity features are often found below volcanic regions and rifts and are interpreted as solidified intrusions [e.g., *Chiarabba et al*., 2000; *Keranen et al*., 2004; *Daly et al*., 2008]. We suggest that the high-velocity body centered beneath Harrat Lunayyir represents a region of solidified magma from previous volcanic episodes, including repeated dyke intrusions that extend to the N-NW. The 2009 dyke intrusion followed this same trend, leading to the observed deformation.

[30] The fast velocity features in our model are generally surrounded by slower velocities (Figure 6). We interpret this to reflect the true crustal velocities beneath Harrat Lunayyir. That is, where volcanic rocks do not intrude, the crust is slower than indicated by broader-scale velocity models for the Arabian Shield [e.g., *Mooney et al*., 1985; *Mokhtar et al*., 1988; *Knox et al*., 1998; *Rodgers et al*., 1999; *Julià et al*., 2003], as represented in our starting model. Crustal velocities increase toward the edges of our model, but the DWS values in these areas are lower and ray coverage is not as complete. The slower crustal *P* wave velocities shown in our model are not unreasonable and in fact compare quite well with global models such as PREM [*Dziewonski and Anderson*, 1981], IASP [*Kennett and Engdahl*, 1991], and ak135 [*Kennett et al*., 1995].

[31] Our earthquake relocations delineate some interesting features throughout the study area as well. Generally, events are deeper in the south and shallower in the north, consistent with preliminary earthquake locations from the SGS [*Baer and Hamiel*, 2010], and the relocations coincide with fast velocity anomalies imaged in our model (Figure 6). In map view, the linear trends of seismicity correspond well with the InSAR-modeled dyke orientation (Figure 9).

[32] To assess any temporal-spatial patterns, we have plotted the earthquake relocations as a function of time (Figure 10). InSAR modeling suggests that 75% of the deformation and the main period of maximum seismic energy release occurred during 8–27 May 2009 [*Pallister et al*., 2010; *Baer and Hamiel*, 2010]. Our seismic data set during these dates is rather limited, but Figure 10 (left) shows that earthquakes occurring during this time were primarily shallow events (~2–8 km) in the northern section of Harrat Lunayyir. Perhaps more interesting is that a majority of all the large magnitude (>3.5) events in our data set occurred during this time. 25% of the deformation occurred during 27 May–28 June, with only negligible deformation in July [*Pallister et al*., 2010; *Baer and Hamiel*, 2010]; however, a considerable number of earthquakes still occurred during this time. Shallow, northern events continued, but deep events (~15 km) beneath southern Harrat Lunayyir also occurred. In mid to late July, a group of intermediate-depth earthquakes developed, connecting the shallow and deep regions of seismicity (Figure 10).

[33] The deformation and stress fields associated with dyke intrusions are complicated and can lead to a variety of failure mechanisms [e.g., *Rubin*, 1992; *Bonafede and Danesi*, 1997; *Rubin et al*., 1998]. To better assess the faulting processes associated with shallow, intermediate, and deep earthquakes from the Harrat Lunayyir swarm, focal mechanisms were computed following an approach similar to *Hansen et al*. [2006]. Cross-correlation values from BCSEIS at reference station KSU1 were used to identify clusters of similar events. Since most of our data are small magnitude earthquakes, grouping them into similar families allows first-motion polarity to be more reliably identified. Individual, larger magnitude (>3.5) events were also examined. Focal mechanisms were computed assuming a double-couple source using FOCMEC [*Snoke et al*., 1984]. For clustered events, the polarity observations and an average hypocenter location for each group were used to generate a composite focal mechanism. While there are variations in the fault plane orientations, earthquakes at all depths (shallow, intermediate, and deep) primarily display normal faulting, consistent with tensional opening (Figure 9). Several strike-slip mechanisms are also observed, which are not uncommon during dike intrusion [*Belachew et al*., 2012; *Shuler and Nettles*, 2012], and they indicate dyke-perpendicular opening. One larger magnitude event also displays a thrust mechanism, but it should be noted that the location of this event is not as well constrained as some of the others (Figure 9).

[34] The imaged velocity structure, the temporal-spatial distribution of the earthquakes, and the corresponding focal mechanisms, in conjunction with InSAR-modeled results, lead to some important interpretations about the 2009 Harrat Lunayyir seismic-volcanic event. During mid to late May, the dyke ascended toward the surface following a N-NW trend marked by solidified magmas from previous intrusions. Shallow earthquakes occurred during this time, including most of the largest magnitude events, and these likely reflect brittle failure above and ahead of the intrusion [*Belachew et al*., 2012; *Shuler and Nettles*, 2012]. From late May to late June, the dyke continued to thicken and lengthen, and shallow events beneath northern Harrat Lunayyir continued. Additionally, deeper earthquakes beneath the southern end of the study region also developed. These may reflect responses to the local stress conditions following the intrusion. It is also interesting to note that the shift from shallow to deep events coincides with the southern termination of the wedge-shaped graben that formed during the episode [Figure 9; *Baer and Hamiel*, 2010]. In mid to late July, toward the end of the seismic swarm, earthquakes at an intermediate depth occurred, connecting the shallow and deep regions of seismicity. It is plausible that this "middle" region was stressed by previous surrounding events and that eventually failure occurred in this area as well.

6. Conclusions

[35] Using DD tomography, we have developed a *P* wave velocity model beneath Harrat Lunayyir in northwestern Saudi Arabia. As part of the joint inversion, earthquakes from

the 2009 seismic swarm have been more precisely located. Our results are unique since harrat magma systems are rarely imaged, and understanding their velocity structure is important in assessing both local tectonics and future seismic and volcanic hazards. Beneath Harrat Lunayyir, fast velocity anomalies have been interpreted as regions marked by repeated volcanic intrusions, oriented NNW-SSE. The crust surrounding the fast intrusions is slower than that suggested by broader-scale models for the Arabian Shield. The largest magnitude earthquakes occurred early in the swarm, concentrated at shallow depths beneath northern Harrat Lunayyir, and these events are associated with the dyke intrusion. Later events include deep earthquakes beneath the southern end of the study area as well as a group of intermediate-depth earthquakes that connect the deep and shallow regions of seismicity. These later events likely represent responses to local stress conditions following the intrusion. Our findings are in agreement with previous studies, which modeled surface deformation in Harrat Lunayyir using InSAR data [*Baer and Hamiel*, 2010; *Pallister et al*., 2010]. Given our observations, coupled with the history of seismic swarms in this region, future volcanic intrusions beneath Harrat Lunayyir seem plausible.

[36] **Acknowledgments.** We thank the National Plan for Science and Technology, KACST-KSU (09-INF945-02), the Saudi Society for Geosciences, and the SGS for providing the necessary funding as well as the earthquake data that made this project possible. We also thank Sigurjón Jónsson, John Pallister, and Gidi Baer for providing the InSAR-modeled feature coordinates from their respective studies and for several helpful discussions, as well as Cindy Ebinger and an anonymous reviewer for their thorough critiques of the manuscript.

References

Aki, K., and W. H. K. Lee (1976), Determination of three-dimensional anomalies under a seismic array using first P arrival times from local earthquakes: 1. A homogeneous intial model, *J. Geophys. Res.*, *81*, 4381–4399.

Al-Amri, A. M. S. (1995), Recent seismic activity in the northern Red Sea, *J. Geodyn.*, *20*, 243–253.

Al-Amri, A. M., M. S. Fnais, K. Abdel-Rahman, S. Mogren, and M. Al-Dabbagh (2012), Geochronological dating and stratigraphic sequences of Harrat Lunayyir, NW Saudi Arabia, *Int. J. Phys. Sci.*, *7*(20), 2791–2805.

Al-Damegh, K., E. Sandvol, and M. Barazangi (2005), Crustal structure of the Arabian plate: New constraints from the analysis of teleseismic receiver functions, *Earth Planet. Sci. Lett.*, *231*, 177–196.

Almond, D. C. (1986), Geological evolution of the Afro-Arabian dome, *Tectonophysics*, *131*, 301–332.

Al-Saud, M. M. (2008), Seismic characteristics and kinematic models of Makkah and central Red Sea regions, *Arab. J. Geosci.*, *1*, 49–61.

Altherr, R., F. Henjes-Kunst, H. Puchelt, and A. Baumann (1990), Volcanic activity in the Red Sea axial trough – Evidence for a large mantle diapir, *Tectonophysics*, *150*, 121–133.

ArRajehi, A., et al., (2010), Geodetic constraints on present-day motion of the Arabian plate, *Tectonics*, *29*, TC3011, doi:10.1029/2009TC002482.

Baer, G., and Y. Hamiel (2010), Form and growth of an embryonic continental rift: InSAR observations and modeling of the 2009 western Arabia rifting episode, *Geophys. J. Int.*, *182*, 155–167.

Belachew, M., C. Ebinger, and D. Coté (2012), Source mechanisms of dike-induced earthquakes in the Dabbahu-Manda Hararo rift segment in Afar, Ethiopia: implications for faulting above dikes, *Geophys. J. Int.*, *192*, 907–917.

Benoit, M. H., A. A. Nyblade, J. C. VanDecar, and H. Gurrola (2003), Upper mantle P wave velocity structure and transition zone thickness beneath the Arabian Shield, *Geophys. Res. Lett.*, *30*(10), 1531, doi:10.1029/2002GL016436.

Bonafede, M., and S. Danesi (1997), Near-field modifications of stress induced by dyke injection at shallow depth, *Geophys. J. Int.*, *130*, 435–448.

Camp, V. E., and M. J. Roobol (1989), The Arabian continental alkali basalt province: Part I. Evolution of Harrat Rahat, Kingdom of Saudi Arabia, *Geol. Soc. Am. Bull.*, *101*, 71–95.

Camp, V. E., and M. J. Roobol (1992), Upwelling asthenosphere beneath western Arabia and its regional implications, *J. Geophys. Res.*, *97*, 15,255–15,271.

Camp, V. E., P. R. Hooper, M. J. Roobol, and D. L. White (1987), The Madinah eruption, Saudi Arabia: Magma mixing and simulataneous eruption of three basaltic chemical types, *Bull. Volcanol.*, *49*, 489–508.

Camp, V. E., M. J. Roobol, and P. R. Hooper (1992), The Arabian continental alkali basalt province: Part II. Evolution of Harrats Khaybar, Ithnayn, and Kura, Kingdom of Saudi Arabia, *Geol. Soc. Am. Bull.*, *103*, 363–391.

Chadwick, W. W., S. Jónsson, D. J. Geist, M. Poland, D. J. Johnson, S. Batt, K. S. Harpp, and A. Ruiz (2011), The May 2005 eruption of Fernandina volcano, Galápagos: The first circumferential dike intrusion observed by GPS and InSAR, *Bull. Volcanol.*, *73*, 679–697.

Chang, S.-J., M. Merino, S. Van der Lee, S. Stein, and C. A. Stein (2011), Mantle flow beneath Arabia offset from the opening Red Sea, *Geophys. Res. Lett.*, *38*, L04301, doi:10.1029/2010GL045852.

Chiarabba, C. A., E. Amato, E. Boschi, and F. Barbari (2000), Recent seismicity and tomographic modeling of the Mount Etna plumbing system, *J. Geophys. Res.*, *105*(B5), 10,923–10,938.

Chu, D., and R. G. Gordon (1998), Current plate motions across the Red Sea, *Geophys. J. Int.*, *135*, 313–328.

Cochran, J. R. (1981), The Gulf of Aden: Structure and evolution of a young ocean basin and continental margin, *J. Geophys. Res.*, *86*, 263–287.

Cochran, J. R., and G. D. Karner (2007), Constraints on the deformation and rupturing of continental lithosphere of the Red Sea, in *Imaging, Mapping, and Modeling Continental Lithosphere Extension and Breakup*, edited by G. D. Karner et al., *Geol. Soc. Spec. Publ.*, *282*, 265–289.

Cochran, J., and F. Martinez (1988), Structure and tectonics of the northern Red Sea: catching a continental margin between rifting and drifting, *Tectonophysics*, *150*, 1–32.

Coleman, R. G., and A. V. McGuire (1988), Magma systems related to the Red Sea opening, *Tectonophysics*, *150*, 77–100.

Coleman, R. G., R. T. Gregory, and G. F. Brown (1983), Cenozoic Volcanic Rocks of Saudi Arabia, U.S. Geol. Surv. Open-file Rep., 83-788, and Saudi Arabian Deputy Minist. Miner. Resourc., Open File Rep., USGS-OF-03-93.

Crosson, R. S. (1976), Crustal structure modeling of earthquake data: 1. Simultaneous least squares estimation of hypocenter and velocity parameters, *J. Geophys. Res.*, *8*, 3036–3046.

Crotwell, H. P., and T. J. Owens (1998), The TauP Toolkit: Flexible Seismic Travel-Time and Raypath Utilities, Version 2.1, University of South Carolina.

Daly, E., D. Keir, C. J. Ebinger, G. W. Stuart, I. D. Bastow, and A. Ayele (2008), Crustal tomographic imaging of a transitional continental rift: the Ethiopian rift, *Geophys. J. Int.*, *172*, 1033–1048.

Debayle, E., J. Lévêque, and M. Cara (2001), Seismic evidence for a deeply rooted low- velocity anomaly in the upper mantle beneath the northeastern Afro/Arabian continent, *Earth Planet. Sci. Lett.*, *193*, 423–436.

Dieterich, J. H. (1988), Growth and persistence of Hawaiian rift zones, *J. Geophys. Res.*, *93*, 4258–4270.

Du, W., C. H. Thurber, and D. Eberhart-Phillips (2004), Earthquake relocation using cross correlation time delay estimates verified with the bispectrum method, *Bull. Seismol. Soc. Am.*, *94*, 856–866.

Dziewonski, A. M., and D. L. Anderson (1981), Preliminary reference Earth model, *Phys. Earth Planet. Inter.*, *25*, 297–356.

Eberhart-Phillips, D. (1986), Three-dimensional velocity structure in Northern California Coast Ranges from inversion of local earthquake arrival times, *Bull. Seismol. Soc. Am.*, *76*, 1025–1052.

Ebinger, C., A. Ayele, D. Keir, J. Rowland, G. Yirgu, T. Wright, M. Belachew, and I. Hamling (2010), Length and timescales of rift faulting and magma intrusion: The Afar rifting cycle from 2005-present, *Annu. Rev. Earth Planet. Sci.*, *38*, 439–466.

El-Isa, Z. H., and A. Al-Shanti (1989), Seismicity and tectonics of the Red Sea and western Arabia, *Geophys. J.*, *97*, 449–457.

Ellsworth, W. L. (1977), Three-dimensional structure of the crust and mantle beneath the island of Hawaii, Ph.D. thesis, Massachusetts Institute of Technology, Boston, Mass.

Farr, T. G., et al. (2007), The Shuttle Radar Topography Mission, *Rev. Geophys.*, *45*, doi:10.1029/2005RG000183.

Gettings, M., H. Blank, W. Mooney, and J. Healey (1986), Crustal structure of Southwestern Saudi Arabia, *J. Geophys. Res.*, *91*, 6491–6512.

Got, J. L., J. Frechet, and F. W. Klein (1994), Deep fault plane geometry inferred from multiplet relative relocation beneath the south flank of Kilauea, *J. Geophys. Res.*, *99*, 15,375–15,386.

Hansen, S. E., S. Y. Schwartz, H. R. DeShon, and V. González (2006), Earthquake Relocation and Focal Mechanism Determination Using Waveform Cross Correlation, Nicoya Peninsula, Costa Rica, *Bull. Seismol. Soc. Am.*, *96*, 1003–1011.

Hansen, S. E., A. J. Rodgers, S. Y. Schwartz, and A. M. S. Al-Amri (2007), Imaging ruptured lithosphere beneath the Red Sea and Arabian Peninsula, *Earth Planet. Sci. Lett.*, *259*, 256–265.

Hansen, S. E., J. B. Gaherty, S. Y. Schwartz, A. J. Rodgers, and A. M. S. Al-Amri (2008), Seismic velocity structure and depth-dependence of anisotropy in the Red Sea and Arabian Shield from surface wave analysis, *J. Geophys. Res.*, *113*, B10307, doi:10.1029/2007JB005335.

Johnson, P. R. (2006), Explanatory Notes to the Map of Proterozoic Geology of Western Saudi Arabia, Saudi Geol. Surv. Tech. Rep., SGS-TR-2006-4, 1:500,000 map.

Jónsson, S. (2012), Tensile rock mass strength estimated using InSAR, *Geophys. Res. Lett.*, *39*, L21305, doi:10.1029/2012GL053309.

Julià, J., C. J. Ammon, and R. B. Herrmann (2003), Lithospheric structure of the Arabian Shield from the inversion of receiver functions and surface-wave group velocities, *Tectonphysics*, *371*, 1–21.

Kennett, B. L. N., and E. R. Engdahl (1991), Travel times for global earthquake location and phase association, *Geophys. J. Int.*, *105*, 429–465.

Kennett, B. L. N., E. R. Engdahl, and R. Buland (1995), Constraints on seismic velocities in the Earth from travel times, *Geophys. J. Int.*, *122*, 108–124.

Keranen, K., S. L. Klemperer, R. Gloaguen, and the EAGLE Working Group (2004), Three- dimensional seismic imaging of a protoridge axis in the Main Ethiopian rift, *Geology*, *32*, 949–952.

Kissling, E. (1988), Geotomography with local earthquake data, *Rev. Geophys.*, *26*, 659–698.

Kissling, E., W. L. Ellsworth, and R. Cockerham (1984), Three-dimensional structure of the Long Valley Caldera, California, region by geotomography, *U.S. Geol. Surv. Open File Rep.*, *84-939*, 188–220.

Kissling, E., W. L. Ellsworth, D. Eberhart-Phillips, and U. Kradolfer (1994), Initial reference models in local earthquake tomography, *J. Geophys. Res.*, *99*, 19,635–19,646.

Kissling, E., S. Husen, and F. Haslinger (2001), Model parameterization in seismic tomography: A choice of consequences for the solution quality, *Phys. Earth Planet. Inter.*, *123*, 89–101.

Knox, R. P., A. A. Nyblade, and C. J. Langston (1998), Upper mantle S velocities beneath the Afar and western Saudi Arabia from Rayleigh wave dispersion, *Geophys. Res. Lett.*, *25*, 4233–4236.

Kumar, M., D. Ramesh, J. Saul, D. Sarkar, and R. Kind (2002), Crustal structure and upper mantle stratigraphy of the Arabian shield, *Geophys. Res. Lett.*, *29*(8), 1242, doi:10.1029/2001GL014530.

Lahr, J. C., B. A. Chouet, C. D. Stephans, J. A. Power, and R. A. Page (1994), Earthquake classification, location, and error analysis in a volcanic environment: implications for the magmatic system of the 1989-1990 eruptions at Redoubt Volcano, Alaska, *J. Volcanol. Geotherm. Res.*, *62*, 137–151.

LeTourneau, P. M., and P. E. Olsen (2003), *The Great Rift Valleys of Pangea in Eastern North America: Tectonics, Structure, and Volcanism*, p. 214, Columbia University Press, New York.

McNutt, S. R. (1996), Seismic monitoring of volcanoes: A review of the state-of-the-art and recent trends, in *Monitoring and Mitigation of Volcano Hazards*, edited by R. Scarpa and R. I. Tilling, pp. 99–146, Springer-Verlag, Berlin, Germany.

Michael, A. J. (1988), Effects of three-dimensional velocity structure on the seismicity of the 1984 Morgan Hill, California, aftershock sequence, *Bull. Seismol. Soc. Am.*, *78*, 1199–1221.

Mokhtar, T. A., R. B. Herrmann, and D. R. Russell (1988), Seismic velocity and Q model for the shallow structure of the Arabian Shield from short-period Rayleigh waves, *Geophysics*, *53*, 1379–1387.

Mooney, W. D., M. E. Gettings, H. R. Blank, and J. H. Healy (1985), Saudi Arabian seismic- refraction profile: a traveltime interpretation of crustal and upper mantle structure, *Tectonophysics*, *111*, 173–246.

Mukhopadhyay, B., S. Mogren, M. Mukhopadhyay, and S. Dasgupta (2012), Incipient status of dyke intrusion in top crust – evidences from the Al-Ays 2009 earthquake swarm, Harrat Lunayyir, SW Saudi Arabia, *Geom. Nat. Hazard. Risk*, *4*, 30–48.

Nyblade, A., Y. Park, A. Rodgers, and A. Al-Amri (2006), Seismic structure of the Arabian Shield Lithosphere and Red Sea Margin, *MARGINS newsletter*, *17*, 13–15.

Pallister, J. S. (1987), Magmatic history of Red Sea rifting, *Geol. Soc. Am. Bull.*, *98*, 400–417.

Pallister, J. S., et al. (2010), Broad accumulation of rift-related extension recorded by dyke intrusion in Saudi Arabia, *Nature Geosci.*, *3*, doi:10.1038/NGEO966.

Park, Y., A. A. Nyblade, A. J. Rodgers, and A. Al-Amri (2007), Upper mantle structure beneath the Arabian Peninsula and northern Red Sea from teleseismic body wave tomography: Implications for the origin of Cenozoic uplift and volcanism in the Arabian Shield, *Geochem. Geophys. Geosyst.*, *8*, Q06021, doi:10.1029/2006GC001566.

Payne, S. J., W. R. Hackett, and R. P. Smith (2009), Paleoseismology of volcanic environments, in *Paleoseismology*, edited by J. P. McCalpin, pp. 271–314, Elsevier, Amsterdam, The Netherlands.

Prodehl, C. (1985), Interpretation of a seismic-refraction survey across the Arabian Shield in Western Saudi Arabia, *Tectonophysics*, *111*, 247–282.

Rodgers, A. J., W. R. Walter, R. J. Mellors, A. M. S. Al-Amri, and Y. Zhang (1999), Lithospheric structure of the Arabian Shield and Platform from complete regional waveform modeling and surface wave group velocities, *Geophys. J. Int.*, *138*, 871–878.

Roobol, M. J. (2009), Geology, Structure and Seismicity of Harrat Lunayyir Volcanic Field, Al- Eis region, northwestern Saudi Arabia, Saudi Geol. Surv. Rep., 14.

Roobol, M. J., K. Bankher, and S. Bamufleh (1994), Geothermal anomalies along the MMN volcanic line including the cities of Al-Madinah, Al-Munawwarah, and Makkah Al-Mukarramah, Saudi Arabian Dep. Minist. Miner. Res. Confid. Rep., DGMR-MADINAH-CR-15-2, 95.

Rubin, A. M. (1992), Dike-induced faulting and graben subsidence in volcanic rift zones, *J. Geophys. Res.*, *97*, 1839–1858.

Rubin, A., D. Gillard, and J. Got (1998), A reinterpretation of seismicity associated with the January 1983 dike intrusion at Kilauea volcano, Hawaii, *J. Geophys. Res.*, *103*, 10,003–10,015.

Rubin, A. M., D. Gillard, and J. L. Got (1999), Streaks of microearthquakes along creeping faults, *Nature*, *400*, 635–641.

Sandvol, E., D. Seber, M. Barazangi, F. Vernon, R. Mellors, and A. Al-Amri (1998), Lithospheric seismic velocity discontinuities beneath the Arabian Shield, *Geophys. Res. Lett.*, *25*, 2873–2876.

Schaff, D. P., G. H. R. Bokelmann, G. C. Beroza, F. Waldhauser, and W. L. Ellsworth (2002), High- resolution image of Calaveras Fault seismicity, *J. Geophys. Res.*, *107*(B9), 2186, doi:10.1029/2001JB000633.

Shearer, P. M. (1997), Improving local earthquake locations using the L1 norm and waveform cross correlation: Application to the Whittier Narrows, California, aftershock sequence, *J. Geophys. Res.*, *102*, 8269–8283.

Shuler, A., and M. Nettles (2012), Earthquake source parameters for the 2010 western Gulf of Aden rifting episode, *Geophys. J. Int.*, *190*, 1111–1122.

Snoke, J. A., J. W. Munsey, A. C. Teague, and G. A. Bollinger (1984), A program for focal mechanism determination by combined use of polarity and SV-P amplitude ratio data, *Earthquake Notes*, *55*, 15.

Stoeser, D. B., and V. E. Camp (1985), Pan-African microplate accretion of the Arabian Shield, *Geol. Soc. Am. Bull.*, *96*, 817–826.

Thurber, C. H. (1981), Earth structure and earthquake locations in the Coyote Lake area, central California, Ph.D. thesis, Massachusetts Institute of Technology, Boston, Mass.

Thurber, C. H. (1992), Hypocenter-velocity structure coupling in local earthquake tomography, *Phys. Earth Planet. Inter.*, *7*, 55–62.

Tkalčić, H., M. Pasyanos, A. Rodgers, R. Gök, W. Walter, and A. Al-Amri (2006), A multistep approach for joint modeling of surface wave dispersion and teleseismic receiver functions: Implications for lithospheric structure of the Arabian Peninsula, *J. Geophys. Res.*, *111*, B11311, doi:10.1029/2005JB004130.

van der Hilst, R. D., and W. Spakman (1989), Importance of the reference model in linearized tomography and images of subduction below the Caribbean plate, *Geophys. Res. Lett.*, *16*, 1093–1096.

van der Hilst, R. D., R. Engdahl, W. Spakman, and G. Nolet (1991), Tomographic imaging of subducted lithosphere below northwest Pacific island arcs, *Nature*, *353*, 37–43.

Waldhauser, F., and W. L. Ellsworth (2000), A double-difference earthquake location algorithm: Method and application to the northern Hayward Fault, California, *Bull. Seismol. Soc. Am.*, *90*, 1353–1368.

Waldhauser, F., and W. L. Ellsworth (2002), Fault structure and mechanics of the Hayward Fault, California, from doube-difference earthquake locations, *J. Geophys. Res.*, *107*(B3), 2054, doi:10.1029/2000JB00084.

Waldhauser, F., W. L. Ellsworth, and A. Cole (1999), Slip-parallel seismic lineations on the northern Hayward Fault, California, *Geophys. Res. Lett.*, *26*, 3525–3528.

Wessel, P., and W. Smith (1998), New, improved version of the Generic Mapping Tools Released, *Eos. Trans. AGU*, *79*, 579.

Zahran, H. M., I. C. F. Stewart, P. R. Johnson, and M. H. Basahel (2002), Aeromagnetic-Anomaly Maps of Central and Western Saudi Arabia, Saudi Geol. Surv. Open-file Rep., SGS-OF-2002-8, scale 1:2,000,000.

Zhang, H., and C. H. Thurber (2003), Double-difference tomography: the method and its application to the Hayward Fault, California, *Bull. Seismol. Soc. Am.*, *93*, 1875–1889.

Zhang, H., C. H. Thurber, and C. Rowe (2003), Automatic P-wave Arrival Detection and Picking with Multiscale Wavelet Analysis for Single-Component Recordings, *Bull. Seismol. Soc. Am.*, *93*, 1904–1912.

Zobin, V. M., A. M. Al-Amri, and M. Fnais (2011), Seismicity associated with active, new-born, and re-awakening basaltic volcanoes: case review and the possible scenarios for the Harrat volcanic provinces, Saudi Arabia, *Arab. J. Geosci.*, *6*, 529–541.